Analysis of two scenarios for the early optical emission of the gamma-ray burst afterglows 990123 and 021211

A. Panaitescu[★] and P. Kumar

Department of Astronomy, University of Texas, Austin, TX 78712, USA

ABSTRACT

The optical light curves of gamma-ray burst (GRB) afterglows 990123 and 021211 exhibit a steep decay at 100–600 s after the burst, the decay becoming slower after about 10 min. We investigate two scenarios for the fast decaying early optical emission of these GRB afterglows. In the reverse–forward shock scenario, this emission arises in the reverse shock crossing the GRB ejecta, the mitigation of the light-curve decay occurring when the forward shock emission overtakes that from the reverse shock. Both a homogeneous and wind-like circumburst medium are considered. In the wind-bubble scenario, the steeply decaying, early optical emission arises from the forward shock interacting with a r^{-2} bubble, with a negligible contribution from the reverse shock, the slower decay starting when the blast wave reaches the bubble termination shock and enters a homogeneous region of the circumburst medium.

We determine the shock microphysical parameters, ejecta kinetic energy and circumburst density, which accommodate the radio and optical measurements of the GRB afterglows 990123 and 021211. We find that, for a homogeneous medium, the radio and optical emissions of the afterglow 990123 can be accommodated by the reverse–forward shock scenario if the microphysical parameters behind the two shocks differ substantially. A wind-like circumburst medium also allows the reverse–forward shock scenario to account for the radio and optical properties of the afterglows 990123 and 021211, but the required wind densities are at least 10 times smaller than those of Galactic Wolf–Rayet stars. The wind-bubble scenario requires a variation of the microphysical parameters when the afterglow fireball reaches the wind termination shock, which seems a contrived feature.

Key words: hydrodynamics – plasmas – radiation mechanisms: non-thermal – shock waves – ISM: jets and outflows – gamma-rays: bursts.

1 INTRODUCTION

There are currently two gamma-ray burst (GRB) afterglows for which a fast falling-off optical emission was detected at early times, only ∼100 s after the burst. The general consensus is that this emission arises from the GRB ejecta which is energized by the reverse shock (RS) crossing the ejecta and caused by the interaction of the ejecta with the circumburst medium (CBM). This interaction also drives a forward shock (FS) energizing the swept-up CBM, to which the later afterglow emission is attributed (the 'reverse–forward shock' scenario).

The RS emission was first calculated by Mészáros & Rees (1997), who considered the cases of a frozen-in and turbulent magnetic field in the ejecta, and showed that, in either case, a bright optical emission ($m_V \sim 9$) is obtained at the end of the burst. Mészáros & Rees (1999) extended their previous calculations of the RS emission to a radiative evolution of the fireball Lorentz factor and pointed out the

importance of spectral information in constraining the RS dynamics and the magnetic field origin from the observed t^{-2} power-law decay of the very early optical light curve of the afterglow 990123 (Akerlof et al. 1999). They also pointed out the possibility that optical flashes arise in the same internal shocks which generate the burst emission.

Sari & Piran (1999) have shown that, if the peak frequency of the RS emission is assumed to be in the optical at the time when the optical emission of the afterglow 990123 peaks (50 s after the burst), then the expected softening of the RS emission and self-absorption effects can account for the radio flare reported by Kulkarni et al. (1999a). Kobayashi & Sari (2000) confirm the RS interpretation of this radio flare through numerical calculations of the RS dynamics.

Chevalier & Li (2000) have presented calculations of the RS synchrotron emission until it crosses the GRB ejecta, for the case of a wind-like CBM. For their choice of a high magnetic field parameter, the RS cooling frequency falls well below the optical domain, which leads to a RS optical emission much dimmer than that observed for the afterglow 990123 at its peak (40 s after the burst). Furthermore,

[★]E-mail: adp@astro.as.utexas.edu

such a low cooling frequency implies that the early afterglow optical emission should cease when the RS has crossed the ejecta shell, i.e. at the peak time of the RS emission. Because this is in contradiction with the observations of the afterglow 990123, Chevalier & Li (2000) have concluded that a wind-like CBM cannot explain the early optical emission of the afterglow 990123.

Constraints on the fireball initial Lorentz factor have been obtained by Soderberg & Ramirez-Ruiz (2003) for several afterglows by comparing the observed radio emission at ∼1 d with the model RS emission, under the assumption that the RS magnetic field and typical electron energy parameters (which we shall call microphysical parameters) are those determined for the FS from fits to the broadband emission of those afterglows (Panaitescu & Kumar 2001). Zhang, Kobayashi & Mészáros (2003) have noted that the ratios of the RS and FS peak fluxes and the peak and cooling frequencies depend only on the fireball initial Lorentz factor and the ratio of the magnetic fields, to develop a method of constraining these two quantities, and have shown that the optical emission of the afterglow 990123 requires a magnetized outflow.

In this paper we use the general properties (flux, epochs during which power-law decays are observed, decay slopes – see Table 1) of the radio and optical emissions of the afterglows 990123 and 021211 to constrain the ejecta (isotropic-equivalent) kinetic energy, CBM density and the microphysical parameters for the reverse–forward shock scenario (Section 4.1), for either a homogeneous or wind-like profile of the CBM. In contrast with other works, we take into account all constraints arising from the radio and optical measurements of the GRB afterglows 990123 and 021211 and we do not assume certain values for any of the model parameters. We also investigate a 'wind-bubble' scenario (Section 5), where all the radio and optical emission arises in the FS, with a negligible contribution from the RS (which is verified numerically), the mitigation of the optical decays observed in the afterglows 990123 and 021211 being due to the FS crossing the bubble termination shock, i.e. transiting from a wind-like CBM structure to a homogeneous region of shocked wind. For both scenarios, we consider either adiabatic or radiative dynamics, and the resulting microphysical parameters are checked for consistency with the assumed dynamical regime.

2 PHYSICAL PARAMETERS AT THE EJECTA SHOCK-CROSSING RADIUS

We begin by calculating the spectral properties (break frequencies and peak flux) of the RS emission at the radius R_+ where the RS finishes crossing the ejecta shell and the injection of fresh electrons by the RS ceases. Because most of the ejecta kinetic energy has been transferred to the forward shock at R_+, the radius R_+ marks the onset of a steeper power-law decrease of the bulk Lorentz factor Γ with radius. After R_+, the spectral properties of the RS emission can

magnetic field. The spectral properties of the FS emission can also be calculated from those at R_+ or directly from the dynamics of the fireball after R_+ (i.e. without passing through the parameters at R_+) if the shock dynamics is adiabatic.

Each shock compresses the fluid ahead of it by a factor $4\Gamma' + 3$, where Γ' is the Lorentz factor of the shocked fluid as measured in the frame of the yet unshocked gas, and heats it to a energy per particle equal to $\Gamma' - 1$. Therefore, the pressure equality at the contact discontinuity, which separates the shocked ejecta and CBM, implies that

$$(4\Gamma' + 3)(\Gamma' - 1)n_{ej} = (4\Gamma + 3)(\Gamma - 1)n \qquad (1)$$

where Γ is the Lorentz factor of the shocked fluid in the laboratory frame, and n_{ej} and n are the proton number densities of the unshocked ejecta and of the CBM, respectively, each measured in the corresponding comoving frame. From the addition of velocities in special relativity,

$$\Gamma' = \Gamma_0\Gamma(1 - \beta_0\beta) \simeq \frac{1}{2}\left(\frac{\Gamma}{\Gamma_0} + \frac{\Gamma_0}{\Gamma}\right) \qquad (2)$$

where Γ_0 is the initial Lorentz factor of the ejecta, β denotes velocities, and $\Gamma_0 \gg 1$ and $\Gamma \gg 1$ were used in the approximation. Substituting equation (2) into equation (1), we obtain a fourth-degree equation for Γ, which can be cast in the form

$$\frac{(\Gamma_0 - \Gamma)^2}{\Gamma\Gamma_0}\left[\frac{(\Gamma_0 + \Gamma)^2}{\Gamma\Gamma_0} - \frac{1}{2}\right]n_{ej} = 4\Gamma^2 n. \qquad (3)$$

Because $\Gamma \leqslant \Gamma_0$, the first term in the square brackets is at least eight times larger than the last term. Ignoring the 1/2 term, the solution of equation (3) is

$$\Gamma = \frac{\Gamma_0}{\left[1 + 2\Gamma_0(n/n_{ej})^{1/2}\right]^{1/2}}. \qquad (4)$$

The limiting cases for the Lorentz factor are

$$\Gamma = \begin{cases} \Gamma_0 & \frac{n_{ej}}{n} \gg 4\Gamma_0^2 \\ \left(\frac{\Gamma_0}{2}\right)^{1/2}\left(\frac{n_{ej}}{n}\right)^{1/4} & \frac{n_{ej}}{n} \ll 4\Gamma_0^2 \end{cases}. \qquad (5)$$

Therefore, in the limit of very dense ejecta, the Lorentz factor of the shocked fluid is the same as that of the unshocked ejecta, while for more tenuous ejecta, Γ depends on the ratio of the comoving densities. Note that the ratio n_{ej} and n_{cmb} changes with the fireball radius R:

$$n_{ej} = \frac{E}{4\pi m_p c^2 \Gamma_0(\Gamma_0\Delta)R^2}, \qquad n = AR^{-s}. \qquad (6)$$

Here, E is the fireball ejecta energy (or, if the outflow is collimated, its isotropic equivalent), m_p is the proton's mass, and $\Delta \ll R$ is

Table 1. Properties of optical and radio emissions used to constrain the afterglow parameters. The columns are as follows: (1) burst redshift; (2) range of burst duration in various X-ray bands; (3) selected epoch for early optical measurement; (4) R-band flux at t_1 (Akerlof et al. 1999; Li et al. 2003); (5) $t_1 - t_2$ temporal index (Li et al. 2003) of the early optical light curve, $F_o \propto t^{-\alpha_{12}}$; (6) last available measurement or end of the steeply falling-off optical afterglow; (7) beginning of slower decaying optical emission; (8) $t_3 - t_4$ optical light-curve index (Kulkarni et al. 1999a; Li et al. 2003), $F_o \propto t^{-\alpha_{34}}$; (9) selected epoch after t_3; (10) R-band flux at t_4 (Fox et al. 2003); (11) slope of optical continuum measured after t_3 (Holland et al. 2000; Pandey et al. 2003) $F_\nu \propto \nu^{-\beta}$; (12) selected epochs of radio measurements; (13) 2σ upper limits on radio fluxes (Kulkarni et al. 1999b; Fox et al. 2003).

GRB	z (1)	t_γ (s) (2)	t_1 (s) (3)	F_1 (mJy) (4)	α_{12} (5)	t_2 (s) (6)	t_3 (7)	α_{34} (8)	t_4 (h) (9)	F_4 (μJy) (10)	β (11)	$t_{5,6,7}$ (d) (12)	$F_{5,6,7}$ (μJy) (13)
990123	1.6	70–100	73	400	1.80	610	4.2h	1.10	8.3	67	0.68–0.82	0.2, 1.2, 4.2	130, 320, 68
021211	1.0	2–8	130	4.1	1.56	650	650s	0.94	2.5	25	0.55–0.98	0.1, 0.9, 3.9	84, 44, 91

the ejecta geometrical thickness measured in the laboratory frame (thus $\Gamma_0 \Delta$ is the comoving frame thickness). We have restricted our calculations to two simple radial structures of the CBM, either homogeneous ($s = 0$) of particle density n or a R^{-2} stratification ($s = 2$) corresponding to a wind expelled by the GRB progenitor. In the latter case, $A = 3 \times 10^{35} A_*$ cm^{-1}, where A_* is the mass-loss rate to wind speed ratio, normalized to 10^{-5} M$_\odot$ yr^{-1}/10^3 km s^{-1}. By denoting

$$X = \frac{E}{4\pi A m_p c^2} \tag{7}$$

the ratio of the comoving densities is

$$\frac{n_{\rm ej}}{n} = \frac{X}{\Delta \Gamma_0^2 R^{2-s}}. \tag{8}$$

The ejecta-shell thickness, Δ, is the largest of its initial thickness $c\tau$, where τ is the laboratory frame duration of the GRB ejecta released by their source, and the expansion due to a spread in the radial outflow velocity of the ejecta particles. This velocity spread can be either a relic of the initial, super-Eddington radiation pressure in the fireball, or an imperfect collimation in the radial direction of the ejecta particles at the end of the fireball acceleration. The former leads to a comoving-frame expansion of the shell at the sound speed, and the latter is expected to produce a spread of order $1/\Gamma_0$ in the ejecta particles direction of motion (Mészáros, Laguna & Rees 1993). In either case, the resulting contribution to the shell thickness evolution is R/Γ_0^2, therefore

$$\Delta = \begin{cases} c\tau & R < 2\Gamma_0^2 c\tau \\ \dfrac{R}{2\Gamma_0^2} & R > 2\Gamma_0^2 c\tau \end{cases}. \tag{9}$$

As shown by Kumar & Panaitescu (2003), the difference between the laboratory frame speeds of the unshocked ejecta and that of the RS is

$$\beta_0 - \beta_{\rm RS} = \frac{1.4}{\Gamma_0^2} \left(\frac{\Gamma_0^2 n}{n_{\rm ej}} \right)^{1/2} \tag{10}$$

for a wide range of the ratio $\Gamma_0^2 \, n/n_{\rm ej}$. From here, we can calculate the radius R_+ at which the RS finishes crossing the ejecta shell:

$$\Delta(R_+) = \int_0^{R_+} (\beta_0 - \beta_{\rm RS}) \, dR. \tag{11}$$

Once R_+ is known, equations (4), (8) and (9) give the Lorentz factor Γ at the shock-crossing radius R_+ and all the properties of the RS and FS emissions at R_+, which can then be extrapolated at $R > R_+$. We proceed by considering separately ejecta shells for which $2\Gamma_0^2 \, c\tau < R_+$ and $R_+ < 2\,\Gamma_0^2 \, c\,\tau$. In the former case, the ejecta shell undergoes a significant spreading while the RS propagates into it, while in the latter case the spreading is negligible. The usual terminology (Sari & Piran 1995) is that of 'thin ejecta' for the former and 'thick ejecta' for the latter.

2.1 Thin ejecta shell: $\Delta = R/(2\Gamma_0^2)$

The substitution of equations (8) and (10) into equation (11) leads to

$$(s = 0): R_+ = \left(\frac{1.6X}{\Gamma_0^2} \right)^{1/3}$$
$$= 0.94 \times 10^{17} \left(\frac{E_{53}}{n_0 \Gamma_{0,2}^2} \right)^{1/3} \text{cm} \tag{12}$$

$$(s = 2): R_+ = \frac{0.57X}{\Gamma_0^2} = 1.0 \times 10^{15} \frac{E_{53}}{A_* \Gamma_{0,2}^2} \text{cm} \tag{13}$$

where the usual notation $Q_n = Q/10^n$ has been used. The defining condition for this case, $R_+ > 2\Gamma_0^2 \, c\tau$, becomes

$$\Gamma_0 < \left[\frac{0.20X}{(c\tau)^3} \right]^{1/8} = 670 \left(\frac{E_{53}}{n_0 \tau_0^3} \right)^{1/8} \quad \text{for } s = 0 \tag{14}$$

$$\Gamma_0 < \left(\frac{0.29X}{c\tau} \right)^{1/4} = 120 \left(\frac{E_{53}}{A_* \tau_0} \right)^{1/4} \quad \text{for } s = 2. \tag{15}$$

From equation (8), the density ratio at R_+ is

$$\frac{n_{\rm ej}}{n}(R_+) = \frac{2X}{R_+^{3-s}} = \begin{cases} 1.3 \, \Gamma_0^2 & s = 0 \\ 3.5 \, \Gamma_0^2 & s = 2 \end{cases}. \tag{16}$$

Compared with equation (4), this shows that at R_+ the Lorentz factor of shocked gas is in an intermediate regime:

$$\Gamma_+ \overset{s=0}{=} 0.60 \, \Gamma_0, \qquad \Gamma_+ \overset{s=2}{=} 0.70 \, \Gamma_0. \tag{17}$$

Besides $\Gamma(R_+)$, two other quantities are of interest at the ejecta shock-crossing radius: the energy of the swept-up CBM, $E_{\rm cbm}(R_+)$, and the corresponding observer frame time, t_+. The total energy of the shocked CBM is Γ^2 larger than its rest-mass energy, thus

$$E_{\rm cbm}(R) = m_p c^2 \int_0^R 4\pi r^2 A r^{-s} \Gamma^2(r) \, dr. \tag{18}$$

The arrival time t corresponding to the contact discontinuity and the fluid moving toward the observer is given by

$$t_{\rm CD}(R) = (1 + z) \int_0^R \frac{dr}{2c\Gamma^2}, \tag{19}$$

where z is the burst redshift. Substituting Γ from equation (4) into equations (18) and (19), we obtain

$$(s = 0): E_{\rm cbm}(R_+) = 0.25E,$$

$$t_+ = 350 \, (1 + z) \left(\frac{E_{53}}{n_0 \Gamma_{0,2}^8} \right)^{1/3} \text{s} \tag{20}$$

$$(s = 2): E_{\rm cbm}(R_+) = 0.34E,$$

$$t_+ = 2.9(1 + z) \frac{E_{53}}{A_* \Gamma_{0,2}^4} \text{s}. \tag{21}$$

Thus, less than half of the initial ejecta energy has been dissipated by the FS by the time the RS crosses the ejecta shell. This means that the shock-crossing radius R_+ is slightly smaller than the usual deceleration radius R_d defined by $E_{\rm cbm}(R_d) = 0.5E$.

2.2 Thick ejecta shell: $\Delta = c\tau$

Once again, using equations (8) and (10) in equation (11), we obtain that

$$R_+ \overset{s=0}{=} (2.0Xc\tau)^{1/4} = 0.24 \times 10^{17} \left(\frac{E_{53} \tau_0}{n_0} \right)^{1/4} \text{cm} \tag{22}$$

$$R_+ \overset{s=2}{=} (0.51Xc\tau)^{1/2} = 0.52 \times 10^{15} \left(\frac{E_{53} \tau_0}{A_*} \right)^{1/2} \text{cm}. \tag{23}$$

The requirement that $R_+ < 2\Gamma_0^2 c\tau$ leads to the reversed inequalities given in equations (14) and (15). The density ratio (equation 8) at R_+ is

$$\frac{n_{\rm ej}}{n}(R_+) = \frac{X}{\Gamma_0^2 c\tau R_+^{2-s}}. \tag{24}$$

Because in the thick shell case the ejecta density is lower than for a thin shell, the values given on the right-hand side of equation (16) are upper limits for the density ratio. Substituting equation (24) in the second regime given in equation (5) leads to

$$(s=0): \Gamma_+ = \left[\frac{X}{32(c\tau)^3}\right]^{1/8} = 530 \left(\frac{E_{53}}{n_0 \tau_0^3}\right)^{1/8} \tag{25}$$

$$(s=2): \Gamma_+ = \left(\frac{X}{4c\tau}\right)^{1/4} = 110 \left(\frac{E_{53}}{A_* \tau_0}\right)^{1/4}. \tag{26}$$

Note from equations (25) and (26) that, for a thick ejecta shell, the Lorentz factor Γ of the shocked ejecta is independent of that of the unshocked ejecta, Γ_0. Thus, for a sufficiently tenuous ejecta, the contrast between Γ_0 and Γ can be sufficiently large that the RS is relativistic (equation 2) in the frame of the incoming ejecta. In contrast, in the thin ejecta case, equations (2) and (17) lead to $\Gamma' - 1 = 0.13$ for $s = 0$ and $\Gamma' - 1 = 0.064$ for $s = 2$, i.e. the RS propagating in a thin ejecta shell is trans-relativistic.

The energy dissipated by the FS at $R = R_+$ and the ejecta shell shock-crossing time are

$$E_{\rm cbm}(R_+) = 0.36E, \qquad t_+ = 0.71(1+z)\tau \tag{27}$$

for either type of medium. Note that, as for a thin ejecta shell, the shock-crossing radius R_+ is close to the usual deceleration radius. Furthermore, for a thick ejecta shell, the observer frame shock-crossing time t_+ is fairly close to the laboratory frame duration of the ejecta release. Given that t_+ is roughly the time-scale for dissipating the ejecta kinetic energy and that, most likely, the shock-accelerated electrons cool faster than the dynamical time-scale, we expect that the duration of an external shock GRB is close to t_+. The simple temporal structure of the GRBs 990123 and 021211 may suggest that they originate in an external shock, nevertheless it is entirely possible that both bursts were produced in internal shocks occurring in an outflow with a fluctuating ejection Lorentz factor (Rees & Mészáros 1994). In this case, the internal shocks take place at the radius $R_{\rm is} \sim \Gamma_{\rm min}^2 c\tau$, where $\Gamma_{\rm min}$ is the Lorentz factor of the slower shells. The shocked fluid moves at $\Gamma \sim (\Gamma_{\rm min}\Gamma_{\rm max})^{1/2}$, where $\Gamma_{\rm max}$ is the Lorentz factor of the faster shells; therefore, the observed burst duration is $t_\gamma = R_{\rm is}/(c\Gamma^2) \sim (\Gamma_{\rm min}/\Gamma_{\rm max})\tau$. Because a high dissipation efficiency requires a large contrast between the Lorentz factors of various ejecta shells ($\Gamma_{\rm min} \ll \Gamma_{\rm max}$), the burst duration sets only a lower limit on the duration of the ejecta release, τ. We shall use this constraint when choosing the shock-crossing time t_+ for the GRBs 990123 and 021211 for the case of a thick ejecta shell.

3 SYNCHROTRON EMISSION

The synchrotron emission from either shock at any observing frequency is determined by the peak flux $F_{\rm p}$, the three break frequencies – absorption $\nu_{\rm a}$, injection $\nu_{\rm i}$ and cooling $\nu_{\rm c}$ – and the slope of the afterglow spectrum between its break frequencies.

The peak of the F_ν synchrotron spectrum, which is at the frequency $\nu_{\rm p} = \min\{\nu_{\rm i}, \nu_{\rm c}\}$, is given by

$$F_{\rm p} = \frac{1+z}{4\pi d_L^2(z)} N_{\rm e} \Gamma P_{\rm p}' \tag{28}$$

where z is the burst redshift, d_L the luminosity distance (in a $H_0 = 70$ km s^{-1} Mpc^{-1}, $\Omega_{\rm M} = 0.3$, $\Omega_\Lambda = 0.7$ universe), $N_{\rm e}$ is the number of radiating electrons, and the factor Γ accounts for the average relativistic boost of the comoving frame synchrotron power $P_{\rm p}'$ per electron at the peak frequency $\nu_{\rm p}' = \nu_{\rm p}/\Gamma$. The Doppler boost Γ appears at only the first power in equation (28) because the observer receives emission for an area subtending an angle of Γ^{-1} radians, i.e. from a fraction Γ^{-2} of the total number of electrons $N_{\rm e}$. Because we will be interested in the early time afterglow emission, the possible collimation of the outflow is not an issue here. After the shock-crossing radius R_+, the number of electrons energized by each shock is

$$N_{\rm e}^{(\rm RS)} = \frac{E}{m_{\rm p}c^2\Gamma_0}, \qquad N_{\rm e}^{(\rm FS)} = \frac{4\pi}{3-s} A R^{3-s}. \tag{29}$$

The comoving power per electron of equation (28) is

$$P_{\rm p}' = \sqrt{3}\phi_{\rm p}\frac{e^3}{m_{\rm e}c^2}B \tag{30}$$

where $\phi_{\rm p}$ is the order-unity coefficient calculated by Wijers & Galama (1999), e is the electron charge, and B is the magnetic field strength. The magnetic field is parametrized by the fraction ε_B of the post-shock energy density stored in it. Taking into account that the FS compresses the CBM by a factor of 4Γ and heats it to an energy per proton of $\Gamma m_{\rm p}c^2$, the magnetic field is

$$B = \left(32\pi\varepsilon_B A R^{-s} m_{\rm p}c^2\Gamma^2\right)^{1/2}. \tag{31}$$

The break frequencies are calculated from the corresponding electron Lorentz factors $\gamma_{\rm a,i,c}$

$$\nu_{\rm a,i,c} = \frac{3x_{\rm p}}{4\pi}\frac{e}{m_{\rm e}c}\gamma_{\rm a,i,c}^2 B\Gamma \tag{32}$$

where $x_{\rm p}$ is another order-unity factor calculated by Wijers & Galama (1999) and the last factor on the right-hand side is for the average relativistic boost of the fireball emission by its relativistic expansion. The typical electron Lorentz factor after shock-acceleration is parametrized as

$$\gamma_{\rm i} = \varepsilon_{\rm i}\frac{m_{\rm p}}{m_{\rm e}}(\Gamma' - 1) \tag{33}$$

where $\Gamma' = \Gamma$ for the FS, while $\Gamma'(R_+)$ for the RS is that given in equation (2) for $\Gamma = \Gamma_+$. We assume that each shock injects in the downstream fluid electrons with a power-law energy distribution

$$\frac{{\rm d}N}{{\rm d}\gamma}(\gamma > \gamma_{\rm i}) \propto \gamma^{-p}. \tag{34}$$

The acceleration of new electrons by the RS ceases at R_+, when all the ejecta have been swept up, but continues at the FS. The cooling electron Lorentz factor is that for which the radiative losses time-scale is equal to the dynamical time-scale:

$$\gamma_{\rm c} = 6\pi\frac{m_{\rm e}c^2}{\sigma_{\rm T}}\frac{\Gamma}{(Y+1)RB^2}. \tag{35}$$

Here, $\sigma_{\rm T}$ is the Thomson cross-section for electron scattering and Y is the Compton parameter, i.e. the ratio of inverse Compton to synchrotron power. The Compton parameter is calculated from the electron distribution, as described by Panaitescu & Kumar (2000). The random Lorentz factor of the electrons radiating at the self-absorption frequency $\nu_{\rm a}$ is given by

$$\gamma_{\rm a} = \begin{cases} \gamma_{\rm p}\tau_{\rm p}^{3/10} & \tau_{\rm p} < 1 \\ \gamma_{\rm p}\tau_{\rm p}^{1/(p+4)} & \tau_{\rm p} > 1 \end{cases}, \qquad \tau_{\rm p} = \frac{5e}{B\gamma_{\rm p}^5}\frac{N_{\rm e}}{4\pi R^2} \tag{36}$$

where $\gamma_{\rm p} = \min\{\gamma_{\rm i}, \gamma_{\rm c}\}$ and $N_{\rm e}$ is given in equation (29).

Equations (28)–(36) provide the characteristics of the RS and FS synchrotron emissions at $R > R_+$, with the values of B, γ_i and γ_c for the RS calculated at $R = R_+$ from equations (31), (33) and (35), respectively (using equations 12, 13, 17, 22, 23, 25 and 26) and then extrapolated at $R > R_+$ as described in Section 3.2. Once $\Gamma(R > R_+)$ is known, the fireball radius can be related with the observer-frame arrival time of the photons emitted at that radius and the evolution of the RS and FS spectral characteristics can be calculated.

The slopes of the piecewise synchrotron spectrum from the broken power-law electron distribution with energy resulting from shock acceleration and radiative cooling are described in detail by Sari, Piran & Narayan (1998). Note that, for $R > R_+$, the RS electron distribution has a sharp cut-off at γ_c, as the injection of electrons stops when the RS has crossed the ejecta shell, which leads to an abrupt switch-off of the RS emission at a given frequency when ν_c drops below that frequency.

3.1 Forward shock

If the dynamics of the FS is adiabatic, the Lorentz factor Γ_F of the FS follows immediately from energy conservation $\Gamma_F^2 M_{cbm} c^2 = E$, where M_{cbm} is the mass of the swept-up CBM. From here we obtain the Blandford–McKee solution (Blandford & McKee 1976):

$$\Gamma_F(R > R_+) = \Gamma_+ \left(\frac{R}{R_+} \right)^{-(3-s)/2}. \tag{37}$$

Equation (19) also gives the photon arrival time for the emission arising from a patch on the FS moving at an angle Γ_F^{-1} relative to the fireball centre–observer axis, from where most of the emission arises. Its integration with Γ from equation (37) leads to

$$t_F(R) = \frac{1+z}{4-s} \frac{R_+}{c\Gamma_+^2} \left[\left(\frac{R}{R_+} \right)^{4-s} + 1 - \frac{s}{2} \right] \tag{38}$$

where the weak deceleration at $R < R_+$ has been ignored in the calculation of the last term on the right-hand side. For $t \gg t_+$, equations (37) and (38) lead to

$$\Gamma_F(t) \propto t^{-(3-s)/(8-2s)}, \qquad R(t) \propto t^{1/(4-s)}. \tag{39}$$

Substituting in equations (29), (31), (33), (35) and (36), we obtain the following scalings

$$F_p \propto t^{-s/(8-2s)}, \qquad \nu_i \propto t^{-3/2} \tag{40}$$

$$\nu_c \propto t^{-(4-3s)/(8-2s)}, \qquad \nu_a \propto t^{-3s/(20-5s)}, \tag{41}$$

where $\nu_a < \nu_i < \nu_c$ was assumed for the last equation. These scalings are used to calculate the characteristics of the FS synchrotron emission at any $t > t_+$ from those at $t = t_+$.

If the swept-up CBM radiates half of its internal energy faster than the dynamical time-scale, the dynamics of the afterglow is described by $\Gamma_F M = \text{const}$, which leads to $\Gamma_F \propto R^{-(3-s)}$. Therefore, the two extreme regimes of the fireball dynamics are

$$\Gamma_F^{(adb)} \propto t^{-(3-s)/(8-2s)}, \qquad \Gamma_F^{(rad)} \propto t^{-(3-s)/(7-2s)}, \tag{42}$$

where the former is the adiabatic case and the latter is a highly radiative regime. To estimate the effect of high radiative losses, we calculate the dependence of the observed flux on the fireball Lorentz factor, $F_\nu \propto \Gamma_F^x$ (with x frequency-dependent), and adjust the fluxes obtained in the adiabatic case by a factor

$$\frac{F_\nu^{(rad)}}{F_\nu^{(adb)}}(t) = \left(\frac{\Gamma_F^{(rad)}}{\Gamma_F^{(adb)}} \right)^x = \left(\frac{t}{t_+} \right)^{-(3-s)x/[(8-2s)(7-2s)]}. \tag{43}$$

The radiative correction factors at $t \sim 0.1$ d are close to those resulting from the expressions of the afterglow flux in the adiabatic case (e.g. equations B1–B9 and C1–C9 in Panaitescu & Kumar 2000) if the fireball energy is decreased by a factor of around 10. This means that a highly radiative regime corresponds to a fractional energy loss of about 90 per cent within the first day after the burst. Note that for such high radiative losses to occur in an afterglow, FS electrons should acquire a substantial fraction of the energy dissipated by the shock and should radiate it quicker than the dynamical time-scale, which requires a sufficiently high magnetic field, i.e. a sufficiently large parameter ε_B and dense CBM.

3.2 Ejecta shell

We calculate the dynamics of the shocked ejecta by assuming adiabatic dynamics and that the ejecta is in equilibrium pressure with the energized CBM, whose radial profile (Lorentz factor, density, pressure) is described by the Blandford–McKee solution. For adiabatic dynamics, the pressure in the ejecta shell evolves as

$$p_R \propto (R^2 \Delta')^{-a} \tag{44}$$

where Δ' is the comoving thickness of the ejecta and a is the adiabatic index. From the Blandford–McKee solution, the pressure equilibrium at the contact discontinuity implies that

$$p_R = p_F(\chi_R) = p_F(\chi = 1)\chi_R^{-(17-4s)/(12-3s)} \tag{45}$$

where $p_F(\chi_R)$ is the pressure of the shocked CBM at the coordinate χ_R of the RS, and

$$p_F(\chi = 1) \propto \Gamma_F^2 n(R) \propto R^{-3} \tag{46}$$

is the pressure immediately behind the FS, the last relation resulting from the dynamics of the FS (equation 37). Equations (44)–(46) imply that the Blandford–McKee coordinate for the RS satisfies

$$\chi_R \propto (R^{2a-3} \Delta'^a)^{3(4-s)/(17-4s)}. \tag{47}$$

Equations (37) and (47) and the Blandford–McKee solution for the post-FS Lorentz factor

$$\Gamma(\chi) \propto \Gamma_F \chi^{-1/2} \tag{48}$$

lead to the Lorentz factor at the location of the contact discontinuity, i.e. the RS Lorentz factor, evolving as

$$\Gamma_R \propto R^{-(3-s)/2} (R^{2a-3} \Delta'^a)^{-1.5(4-s)/(17-4s)}. \tag{49}$$

The adiabatic index a (equation 49) of the ejecta is initially $4/3$ if the RS is relativistic, which corresponds to the thick ejecta case discussed in Section 2.2, and lower for a mildly relativistic shock (thin ejecta – Section 2.1), decreasing to $5/3$ due to the ejecta cooling. Between these limiting cases, the exponents of R and Δ' given in equation (49) change by 0.24 and 0.14, respectively. Such variations do not lead to significant changes in the solutions presented in Section 4.1. For ease of further calculations, we will use $a = 1.5$ in equation (49).

The only uncertainty left in the evolution of Γ_R is that of the ejecta shell comoving thickness Δ'. This uncertainty also affects the adiabatic cooling of the electrons and the evolution of the magnetic field in the ejecta. The evolution of the electron Lorentz factors γ_i and γ_c at $R > R_+$ is

$$\gamma_{i,c} \propto V'^{-(a_e-1)} \propto (R^2 \Delta')^{-1/3} \tag{50}$$

where V' is the comoving frame ejecta volume and an adiabatic index $a_e = 4/3$ for the relativistic electrons has been used for the last term. Because the ejecta emission switches off when the decreasing

cooling frequency $\nu_c^{(RS)}$ falls below the observing frequency ν, we will search for afterglow parameters for which $\nu_c^{(RS)}(t_{\max}) > \nu$, where $t_{\max}$ is the latest time when the RS emission was (or was thought to have been) observed. Therefore, the electrons radiating at frequency ν cool mostly adiabatically and the ejecta radiative cooling after R_+ can be ignored. For the magnetic field, the flux-freezing condition yields

$$B_\perp \propto (R\Delta')^{-1}, \qquad B_\parallel \propto R^{-2} \tag{51}$$

where $B_\perp (B_\parallel)$ is the magnetic field perpendicular (parallel) to the radial direction of the fireball motion.

To assess the effect of the uncertainty of the behaviour of Δ' on the ejecta synchrotron emission, we consider two extreme cases: $\Delta' = $ const, as could result from the compression ejecta against the decelerating contact discontinuity, and $\Delta' = R/\Gamma_R$, corresponding to a comoving-frame expansion of the ejecta shell at a speed comparable to the speed of light. For the former case, relating the ejecta radius with the observer time through $R \propto \Gamma_R^2 t$, leads to $R \propto t^{1/4}$ for $s = 0$ and $R \propto t^{1/2}$ for $s = 2$ (just as for the FS). Substituting in equation (52) shows that $B_\perp \propto R^{-1}$ decays slower than $B_\parallel$. Then, equations (28), (32), (36) and (50) yield

$$(s = 0) \quad F_p \propto t^{-0.63}, \quad \nu_{i,c} \propto t^{-0.96}, \quad \nu_a \propto t^{-0.61} \tag{52}$$

$$(s = 2) \quad F_p \propto t^{-0.75}, \quad \nu_{i,c} \propto t^{-1.42}, \quad \nu_a \propto t^{-0.72}. \tag{53}$$

For an ejecta shell spreading law $\Delta' = R/\Gamma_R$, we obtain that $R \propto t^{1/9}$ for $s = 0$ and $R \propto t^{1/5}$ for $s = 2$. Equation (51) shows that $B_\parallel \propto R^{-2}$ decays slower than $B_\perp$, leading to

$$(s = 0) \quad F_p \propto t^{-0.67}, \quad \nu_{i,c} \propto t^{-1.19}, \quad \nu_a \propto t^{-0.41} \tag{54}$$

$$(s = 2) \quad F_p \propto t^{-0.80}, \quad \nu_{i,c} \propto t^{-1.47}, \quad \nu_a \propto t^{-0.47}. \tag{55}$$

From the above scalings, it can be seen that the temporal index of the break frequencies changes by ~ 0.2 (0.05–0.25) for $s = 0$ ($s = 2$), while that of the peak flux changes by 0.05 for either type of medium. The solutions presented in Section 4.1 vary little between the above assumed behaviours of Δ'.

Equations (54) and (55) are used to calculate the characteristics of the RS synchrotron emission at $t > t_+$ from those at t_+. The effect of radiative losses on the RS emission is estimated in a similar way as for the FS (equation 43), by adjusting the fluxes obtained in the adiabatic case by a factor which accounts for the faster deceleration of the FS due to the radiative losses. For the highly radiative regime, the evolution of the RS Lorentz factor Γ_R is calculated as in the adiabatic case (equations 44 and 49) but using the scaling of the FS Lorentz factor Γ_F with radius corresponding to the radiative dynamics case (equation 42).[1] The absorption of the RS radio emission in the FS is also taken into account.

4 REVERSE-FORWARD SHOCK SCENARIO

The formalism presented in Sections 2 and 3 allows the calculation of the RS and FS emission at a given observer time and observing frequency. These emissions depend on the dynamics of the FS and ejecta shell, i.e. on the fireball kinetic energy E and the particle density of the CBM (n for a homogeneous medium or A_* for a wind surrounding a massive star). The ejecta-shell shock-crossing time t_+ also depends on the fireball initial Lorentz factor Γ_0, for thin

ejecta, or on the duration τ of the fireball ejection, for thick ejecta. The initial Lorentz factor also determines the number of electrons in the ejecta and, therefore, the RS emission. Finally, the RS and FS emissions depend on the two microphysical parameters ε_i and ε_B which quantify the typical electron energy and the magnetic field. Thus, the RS emission is determined by five parameters in the thin ejecta case, or six in the opposite case, while the FS emission depends on four parameters. Note that E and n (or A_*) determine the emission of both shocks.

In this section we determine, in the framework of the reverse–forward shock scenario, the values of the above parameters allowed by the radio and optical emissions of the GRB afterglows 990123 and 021211, the only two afterglows for which an optical emission has been detected at early times, ~ 100 s after the burst.

Table 1 lists the properties of the burst, optical and radio emissions of the two afterglows. For the afterglow 021211, the optical emission is decaying since the first measurement, at $t_1 = 130$ s after the burst (Li et al. 2003). For the afterglow 990123, the emission begins to decay at ~ 45 s (Akerlof et al. 1999), after which the burst exhibits some variability. This raises the possibility of some energy injection in the RS after 45 s. For this reason, we choose $t_1 = 73$ s as the beginning of the afterglow decay, as after this epoch the burst exhibits a weaker, decaying emission.

In both cases, the early optical emission falls off steeper than at later times. For the afterglow 021211, the transition between these two regimes has been observed: it occurs at $t_* = 550$–750 s (Li et al. 2003). For GRB 990123, the transition is inferred to occur at $t_* = 400$–700 s (Li et al. 2003), i.e. around or after the last early optical measurement at $t_2 = 610$ s (Akerlof et al. 1999) but prior to the next available measurement at $t_3 \sim 4.0$ h after the burst (Kulkarni et al. 1999b).

4.1 Constraints on the FS and RS emissions

The slower decaying optical emission lasting for days is naturally attributed to the FS energizing the CBM. Its t^{-1} decay implies that the FS injection frequency is below the optical domain at the first epoch, t_3, when the slower decay begins:

$$\nu_i^{(FS)}(t_3) < 5 \times 10^{14} \text{ Hz} \quad \text{(constraint 1)}. \tag{56}$$

A second constraint is set by the optical flux normalization; for this we choose an epoch $t_4 > t_3$ when the model flux, $F_o^{(FS)}$, is required to be within a factor of 3 of the observed flux, $F_o^{(obs)}$, making allowance for some uncertainty in our calculations: [2]

$$\frac{1}{3} F_o^{(obs)}(t_4) < F_o^{(FS)}(t_4) < 3 F_o^{(obs)}(t_4) \quad \text{(constraint 2)}. \tag{57}$$

With the exception of the flare seen at $t = 1.2$ d in the radio afterglow of GRB 990123, there are no other detections in the radio down to 0.1 mJy or less. We use the 2σ upper limits on the radio flux at three epochs ($t_{5,6,7}$) spanning the interval 0.1–4 d, to constrain the radio FS emission, $F_r^{(FS)}$:

$$F_r^{(FS)}(t_{5,6,7}) < F_r^{(2\sigma)}(t_{5,6,7}) \quad \text{(constraint 3)}. \tag{58}$$

That the early afterglow exhibits a steep fall-off requires that the RS has crossed the ejecta. The burst duration, t_γ, sets a lower bound

---

[1] Because the calculation of Γ_R makes use of the Blandford–McKee solution for adiabatic dynamics, our calculation of Γ_R for radiative dynamics is only a crude approximation.

[2] This uncertainty factor determines the width of the region of allowed $\varepsilon_i - \varepsilon_B$ solutions in the lower-left corner–upper-right corner direction in the figures, and does not affect significantly the conclusions that will be drawn.

on the ejecta crossing time t_+, as discussed in Section 2.2, thus t_+ is constrained by

$$t_\gamma < t_+ < t_1 \quad \text{(constraint 4).} \tag{59}$$

Furthermore, the steep $t^{-1.6}$ decay of the RS emission at t_1 requires that the RS injection frequency is below the optical domain at that time:

$$\nu_i^{(RS)}(t_1) < 5 \times 10^{14} \text{ Hz} \quad \text{(constraint 5).} \tag{60}$$

Matching the observed flux to within a factor of 3,

$$\frac{1}{3} F_o^{(obs)}(t_1) < F_o^{(RS)}(t_1) < 3 F_o^{(obs)}(t_1) \quad \text{(constraint 6),} \tag{61}$$

is another requirement set on the calculated RS emission. The detection of RS emission until epoch t_2, when the early observations end (GRB 990123) or when the transition to the FS emission is observed (GRB 021211), implies that the RS cooling frequency remains above the optical domain until at least epoch t_2:

$$\nu_c^{(RS)}(t_2) > 5 \times 10^{14} \text{ Hz} \quad \text{(constraint 7).} \tag{62}$$

Otherwise, the RS optical emission would exhibit a sharp drop when $\nu_c^{(RS)}$ falls below optical. Finally, the radio upper limits are imposed on the RS emission as well:

$$F_r^{(RS)}(t_{5,6,7}) < F_r^{(2\sigma)}(t_{5,6,7}) \quad \text{(constraint 8).} \tag{63}$$

We search for afterglow parameters $(\Gamma_0, E; n/A_*; \varepsilon_i, \varepsilon_B)$ that lead to FS and RS emissions satisfying the constraints 1–3 and 5–8, respectively. For GRB 990123, constraint 4 requires that $t_+ \sim 70$ s, as for this burst $t_\gamma \sim t_1$. For GRB 021211, the same constraint allows that $4 < t_+ < 130$ s. In the thin ejecta case, t_+ determines the ejecta initial Lorentz factor, Γ_0 (equations 20 and 21). For thick ejecta, t_+ determines the duration of the ejecta release, τ (equation 27). Note that, in the case of a thick ejecta shell, the reversed inequalities given in equations (14) and (15) provide only a lower limit on Γ_0. Nevertheless, Γ_0 remains a relevant parameter because it sets the number of electrons in the ejecta.

The index p of the electron energy distribution (equation 34) is determined from the exponent α of the optical power-law decay, $F_\nu \propto t^{-\alpha}$, for each shock. The available measurements of the slope β of the optical continuum, $F_\nu \propto \nu^{-\beta}$, at $t \sim 1$ d, constrain the index p through the fact that the intrinsic afterglow spectral slope β_o cannot be larger than observed, as intrinsic spectra harder than observed ($\beta_o < \beta$) can be attributed to dust reddening in the host galaxy.

4.2 Results

The search for afterglow parameters is performed by choosing various combinations of parameters (E, n) (for $s = 0$) or (E, A_*) (for $s = 2$) and by identifying the regions in the $(\varepsilon_i, \varepsilon_B)$ parameter space which satisfy the above constraints. Various values of the initial Lorentz factor Γ_0 satisfying constraint 4 are tried, to maximize the allowed $(\varepsilon_i, \varepsilon_B)$ parameter range. For thin ejecta, the $(E, n/A_*; \varepsilon_i, \varepsilon_B)$ parameter space for the RS is significantly smaller than for thick ejecta. For brevity, we present here only solutions for the latter case.

Figs 1–3 show the RS and FS solutions $(\varepsilon_i, \varepsilon_B)$ for various combinations (E, n) or (E, A_*) for which both RS and FS solutions exist. For parameters E, n (or A_*) different by a factor of 10 than those shown, the emission from one of the shocks, or from both, fails to satisfy the above constraints. For all these three figures, the adiabatic index in the shocked ejecta (Section 3.2) was set to $a = 1.5$ and the comoving thickness of the ejecta was assumed to evolve as

$\Delta' = R/\Gamma_R$, where Γ_R is the bulk Lorentz factor of the shocked ejecta at $R > R_+$. Taking $a = 4/3$, as for a relativistic RS, or assuming a constant Δ' lead to a modest change in the solutions shown and leave unaltered the conclusions below. To assess the effect of radiative losses, the fluxes obtained in the adiabatic case were decreased as expected from the faster deceleration of Γ in the case of radiative dynamics (equation 43).

For the reverse–forward shock scenario, we reach the following conclusions about the RS and FS parameters

(i) GRB 990123, homogeneous CBM (Fig. 1). RS and FS microphysical parameters differ, with $\varepsilon_B^{(RS)} \gtrsim 100 \, \varepsilon_B^{(FS)}$ and $\varepsilon_i^{(RS)} < 0.1 \varepsilon_i^{(FS)}$. A RS magnetic field larger than that behind the FS points to an ejecta which was initially magnetized. FS solutions correspond to a cooling frequency, $\nu_c^{(FS)}$, above the optical domain. The power-law decay of the FS optical light curve, α_{34}, sets the electron index: $p = (4\alpha_{34} + 3)/3 = 2.47 \pm 0.07$. This implies that the slope of the intrinsic optical continuum is $\beta_o = (p - 1)/2 = 0.74 \pm 0.04$, consistent with the value reported by Holland et al. (2000), at $t = 1$–3 d after the burst. FS solutions are obtained only for high radiative losses. For the FS parameters shown in Fig. 1, the ratio of the (inverse-Compton) cooling to injection electron Lorentz factors is $\gamma_c/\gamma_i \sim 10 \, (t/0.1 \, \text{d})^{2/3}$, therefore the energy given to electrons which cool radiatively ($\gamma > \gamma_c$) is a fraction $f(t) = (\gamma_c/\gamma_i)^{2-p} = 0.34 \, (t/0.1 \, \text{d})^{-1/3}$ of the total electron energy. If the injected electron distribution extends to arbitrarily high energies, the fraction of the post-shock energy in electrons is $\epsilon_e = [(p - 1)/(p - 2)] \, \varepsilon_i = 3 \, \varepsilon_i \in (0.3, 1)$. Then, at $t = 0.1$ d, the radiative losses over one dynamical time-scale are a fraction $\xi_{rad}(0.1 \, \text{d}) = f \epsilon_e \simeq \varepsilon_i \in (0.1, 0.3)$ of the FS energy. If the total electron energy does not exceed equipartition ($\epsilon_e \leqslant 0.5$), then $\xi_{rad}(0.1 \, \text{d}) \lesssim 0.15$. Therefore, for the FS solutions shown in Fig. 1, the fireball dynamics is between the adiabatic and highly radiative regimes.

The ejecta kinetic energy $E \gtrsim 10^{55}$ erg (if spherical) and the ambient medium density $n \gtrsim 0.1 \, \text{cm}^{-3}$ for which the RS emission accommodates the early optical emission of the afterglow 990123 are 10 and 50 times larger than their upper limits found by us (Panaitescu & Kumar 2001) from multiwavelength afterglow modelling. The difference is caused by the inclusion in the current calculations of the early ($t < t_*$) optical emission, which cannot be accommodated by the RS if the fireball energy and CBM density were those determined from modelling the afterglow emission at $t > 4$ h, as the constraints 6 and 8 in Section 4.1 cannot be satisfied simultaneously. Conversely, for the (E, n) values for which the RS emission accounts for the early optical emission, the FS solutions identified in this paper satisfy the general constraints imposed by observations (Section 4.1) but provide a χ^2-wise poorer fit to the afterglow data after 4 h than the best fit obtained numerically with more accurate calculations of radiative losses and the integration of received emission over the photon equal arrival time surface.

(ii) GRB 990123, r^{-2} CBM (Fig. 2). There are RS and FS solutions with the same microphysical parameters. RS solutions exist only for radiative dynamics. Denser wind environments are found to allow RS solutions if the kinetic energy E is increased, but even for $E = 10^{56}$ erg, which is 30 times larger than the GRB output, the allowed wind density is well below that of a Wolf–Rayet (WR) star ($A_* \simeq 1$). FS solutions correspond to $\nu_c^{(FS)}$ above the optical domain, therefore the electron index is $p = (4\alpha_{34} + 1)/3 = 1.83 \pm 0.08$, leading to $\beta_o = (p - 1)/2 = 0.42 \pm 0.04$, i.e. significantly harder than any reported measurement. The RS and FS solutions shown in Fig. 2 with $\varepsilon_i \sim 10^{-2}$ are consistent with high radiative losses if electrons reach equipartition ($\epsilon_e = 0.5$), because $p < 2$
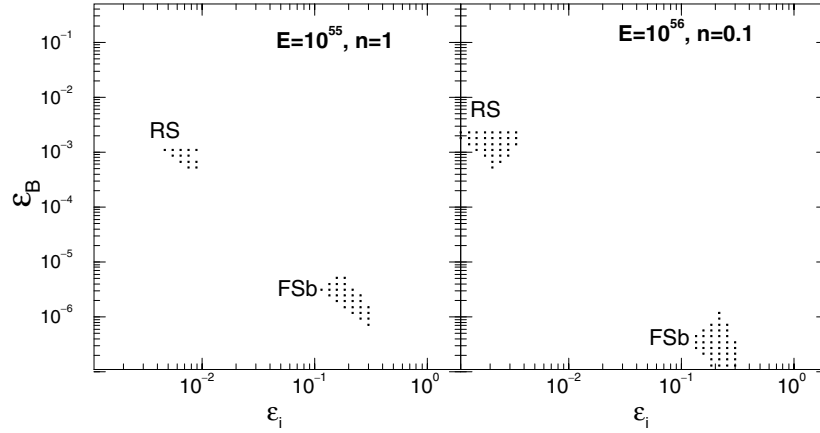
Figure 1. Reverse–forward shock scenario, GRB 990123, homogeneous CBM. Reverse and forward shock microphysical parameters (ε_i, ε_B) for the minimal electron energy and magnetic field energy, satisfying the constraints described in Section 4.1. An uncertainty of a factor of 3 is assumed in the calculated optical fluxes; however, no uncertainty factor is assigned to the analytical radio fluxes, as they are compared with 2σ observational upper limits. 'RS' and 'FSb' denote reverse and forward shock solutions, respectively, the FS solutions corresponding to a cooling frequency above (blueward of) the optical domain. The solutions shown are for thick ejecta (Section 2.2), with an observer-frame RS ejecta crossing time $t_+ = 70$ s, and for highly radiative dynamics (Section 3.1). There are no FS solutions for adiabatic dynamics. Each panel specifies the isotropic-equivalent of the blast-wave kinetic energy, E (in erg), and CBM particle density, n (in cm^{-3}). For values of (E, n) differing by a factor of 10 or more than those shown here, the emission of at least one of the shocks becomes incompatible with the observations. For comparison, the isotropic equivalent of the gamma-ray output of this burst is $E_\gamma = 3 \times 10^{54}$ erg (Kulkarni et al. 1999b).
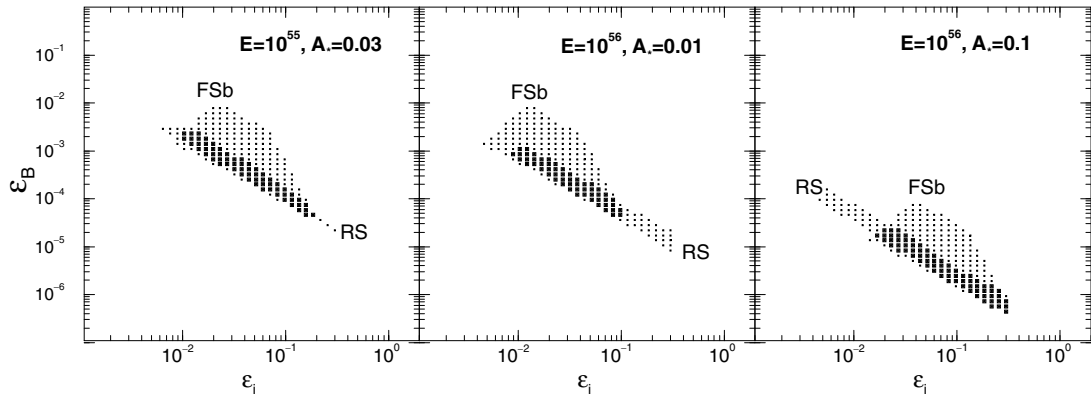

Figure 2. Reverse–forward shock scenario, GRB 990123, wind-like CBM. Solutions for radiative dynamics and a CBM shaped by the wind blown by a massive star. The parameter A_* parametrizes the wind particle density $n(r) = \dot{M}/(4\pi m_p r^2 v_w) = 3 \times 10^{35} A_* r_{cm}^{-2}$, where $\dot{M}$ is the mass-loss rate and v_w is the wind velocity, with $A_* = 1$ corresponding to $\dot{M}/v_w = 10^{-5}$ M$_\odot$ yr^{-1}/10^3 km s^{-1}. Higher values of A_* than shown here, such as those expected for WR stars ($A_* \simeq 1$), do not allow RS solutions, for either adiabatic or radiative dynamics. Overlapping FS and RS solutions are shown with larger symbols. There are no RS solutions for adiabatic dynamics.

allows most of the electron energy to be at $\gamma > \gamma_c$. However, for the solutions with $\varepsilon_i \sim 0.1$, equipartition energies require a cut-off in the accelerated electron distribution at $\gamma_{cut} < \gamma_c$. The synchrotron characteristic frequency for the γ_{cut} electrons is above the optical domain (thus the cut-off does not affect the optical afterglow), but $\gamma_{cut} < \gamma_c$ implies that all injected electrons are cooling adiabatically, i.e. the assumption of high radiative losses becomes invalid for $\varepsilon_i \gtrsim 0.1$.

(iii) GRB 021211, homogeneous CBM. In our previous study (Kumar & Panaitescu 2003) we have shown that, in the thin ejecta shell case, the RS magnetic field parameter must be 10^3–10^4 times larger than for the FS. For a thick ejecta shell, corresponding to a RS shell-crossing time longer than the burst duration (2–8 s) but shorter than the time of the first optical measurement (130 s), there are RS and FS solutions with the same microphysical parameters if the dynamics is radiative.

(iv) GRB 021211, r^{-2} CBM (Fig. 3). RS and FS may have the same microphysical parameters, for either adiabatic or radiative dynamics. There are also solutions with the same parameter ε_i and a RS magnetic field parameter larger than for the FS, indicative of a frozen-in magnetic field. FS solutions correspond to $\nu_c^{(FS)}$ above the optical domain, leading to $p = 1.59 \pm 0.08$ and $\beta_o = 0.29 \pm 0.04$, which is 2σ below the hardest slope reported (Pandey et al. 2003, at $t = 20$ h). Because $p < 2$, the dynamics may be radiative for $\varepsilon_i < 0.1$ and $\epsilon_e = 0.5$, while a significantly lower ϵ_e would ensure an adiabatic dynamical regime. Note that a high $E = 10^{54}$ erg, more than 100 times larger than the burst output, is required by a wind density corresponding to $A_* = 0.3$, i.e. slightly below that of a WR star. From the constraints on the FS parameters, Chevalier, Li & Fransson (2004) have also concluded that a weak wind with $A_* \sim 0.01$ is required for the afterglow 021211; however, in their calculations, the FS cooling frequency was placed below the optical.
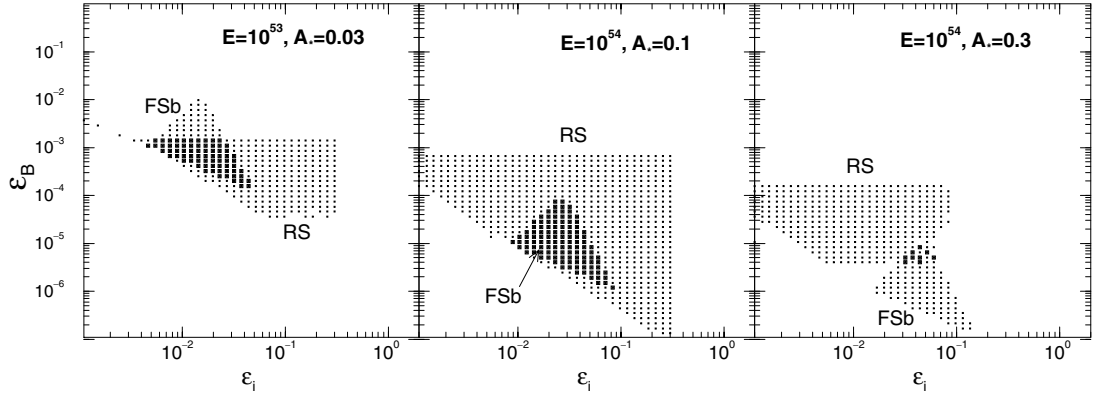
Figure 3. Reverse–forward shock scenario, GRB 021211, wind-like CBM. Solutions for radiative dynamics and $t_+ = 100$ s. Adiabatic dynamics also allows solutions with the same microphysical parameters behind the shocks. There are no RS solutions for denser winds (larger A_*), or fireball energies $E \lesssim 3 \times 10^{52}$ erg, for either adiabatic or radiative dynamics. The isotropic-equivalent gamma-ray output of this burst is $E_\gamma = 6 \times 10^{51}$ erg (Vreeswijk et al. 2002).

If we impose the same constraint here, we do not find any solutions for the RS microphysical parameters.

5 WIND-BUBBLE SCENARIO

The similarity of the decay indices of the optical light curves of the afterglows 990123 and 021211 before and after $t_* \sim 600$ s may suggest that a single mechanism produces the entire optical afterglow emission. Time-varying microphysical parameters, including the slope of the power-law electron energy distribution, could cause a change in the optical light-curve decay index; however, such an explanation is in contradiction with the consistency seen in many afterglows between the optical spectral slope and light-curve decay index at times of the order of 1 d.

If the FS is the only mechanism producing the detected afterglow emission and if microphysical parameters are constant, then the non-monotonic behaviour of the optical light curves of the afterglows 990123 and 021211 at $t_* \sim 600$ s must be tied with the fireball dynamics. The fireball dynamics is determined by the ejecta initial energy and CBM density. A substantial energy injection can mitigate the afterglow dimming rate; however, the energy deposition would have to last for the entire duration of the slower power-law decay, i.e. until at least a few days, and could lead to a too bright radio emission from the RS.

Besides energy injection, a sudden variation in the radial profile of the CBM could also alter the afterglow behaviour. Such a variation is suggested by the association of GRBs with the death of massive stars, which drive powerful winds, and that the modelling of multiwavelength afterglow measurements starting a few hours after the burst leads to better fits for a homogeneous medium than a wind. This discrepancy may be resolved if the afterglow does not arise in a freely expanding wind, but in the environment resulting from the interaction of the wind with the circumstellar gas (Wijers 2001) or with the winds blown by other stars (Scalo & Wheeler 2001). It is then possible that the GRB ejecta run into a CBM whose density profile at smaller radii is the r^{-2} expected for a uniform, free wind, and closer to uniformity at larger distances. Then, if the FS cooling frequency is above the optical domain, the optical afterglow light-curve index should decrease by $\delta \alpha = 0.5$ when the wind termination shock is reached. The resulting index decrease is slightly smaller than observed, but it is possible that deviations from uniformity of the environment outside the unperturbed wind account for the difference.

One important issue for this wind-bubble scenario is under what conditions the wind termination shock is located at the radius R_* of the afterglow at the time t_* when the light curve transits from a steeper to a slower decay. From equations (13) and (38), we obtain

$$R_* \sim 1.4 \times 10^{16} \left(\frac{E_{53}}{A_*} \frac{t_*}{600 \text{ s}} \frac{2}{1+z} \right)^{1/2} \text{ cm.} \qquad (64)$$

R_* is higher by a factor of a few for the wind parameters $A_* \sim 0.1$ which we find for this scenario, and by an extra factor $\gtrsim 10$ for the high ejecta kinetic energy obtained for the afterglow 990123. Thus, we shall find that $R_* \sim 0.3$ pc for the afterglow 990123 and $R_* \lesssim 0.02$ pc for the afterglow 021211. Because the afterglow radius increases as $R \propto t^{1/4}$ at $R > R_*$ and because the slower decay of the afterglows 990123 and 021211 is seen from $t = t_*$ until $t \sim$ a few days, the uniform part of the CBM must extend up to at least $5\,R_*$.

Castor, McCray & Weaver (1975) have derived the major physical properties of a bubble resulting from the interaction of stellar winds with the interstellar gas, taking into account the cooling and the diffusion of the interstellar gas into the shocked wind. The radius of the wind termination shock R_t can be estimated from the equality of the wind ram pressure and that inside the bubble, leading to $R_t = 4 \, \dot{M}_{-5}^{0.3} v_{w,3}^{0.1} n_0^{-0.3} t_5^{0.4}$ pc, where $\dot{M}_{-5}$ is the mass-loss rate in 10^{-5} M$_\odot$ yr^{-1}, $v_{w,3}$ is the wind velocity in km s^{-1}, n_0 is the interstellar gas density in cm^{-3}, and t_5 is the duration of the wind measured in 10^5 yr. From here, the ratio of the contact discontinuity radius R_{cd} to that of the wind termination shock is $R_{cd}/R_t = 2.3 \, \dot{M}_{-5}^{-0.1} v_{w,3}^{0.3} n_0^{0.1} t_5^{0.2}$. Thus, for a GRB occurring in a dense cloud ($n > 10^5$ cm^{-3}), the termination shock radius could be at a location required by the CBM scenario (equation 64) and the shocked wind shell could be sufficiently thick.

However, WR winds do not interact with the interstellar medium but with the wind expelled during the red supergiant (RSG) phase, which collides with the main-sequence phase wind decelerated by the interaction with the interstellar medium. The numerical hydrodynamical calculations of Ramirez-Ruiz et al. (2001) take into account the wind history and show that $R_t \sim 0.02$ pc for $n = 1$ cm^{-3} and $t = 10^6$ yr. Such a termination shock radius is suitable for the wind-bubble scenario and the afterglow 021211, however the wind-bubble size (0.3 pc) shown by Ramirez-Ruiz et al. (2001) is surprisingly small, being 100 times less than that expected from the analytical results of Castor et al. (1975). Chevalier et al. (2004) have considered the possibility that a high interstellar pressure may stall the

bubble expansion. For the external pressure expected in an intense starburst region, their numerical simulations lead to a wind shock termination radius $R_t = 0.4$ pc and a contact discontinuity located at $R_{cd} = 4R_t$, which is about right for the wind-bubble scenario and the afterglow 990123.

Alternatively, the uniformity of the CBM at $R > R_*$ required by the wind-bubble scenario might arise from a sudden increase in the wind speed, leading to an inner shock propagating into the incoming wind. The self-similar solutions derived by Chevalier & Imamura (1983) for colliding winds show that a thick, uniform density shell forms behind the inner shock if the termination shock moves at less than 1 per cent of the unshocked wind speed, which requires the fluctuation in the wind to consist of a decrease in the mass-loss rate by a factor of 100 and an increase of the wind speed increases by a factor of 100 or larger. Such a dramatic change in the wind properties exceeds that expected at the transition from a luminous blue variable (LBV) wind ($\dot{M} \gtrsim 10^{-3}\,M_\odot\,\mathrm{yr}^{-1}$, $v_w = 200\,\mathrm{km\,s^{-1}}$; Garcia-Segura, Mac Low & Langer 1996a) or a RSG wind ($\dot{M} = 10^{-4}\,M_\odot\,\mathrm{yr}^{-1}$, $v_w \lesssim 100\,\mathrm{km\,s^{-1}}$; Garcia-Segura, Langer & Mac Low 1996b) to a WR wind ($\dot{M} = 10^{-5}\,M_\odot\,\mathrm{yr}^{-1}$, $v_w \gtrsim 1000\,\mathrm{km\,s^{-1}}$). The inner shock speed $v_{sh} = v_w^{(WR)}/100 = 10\,\mathrm{km\,s^{-1}}$ and the location of the termination shock required by the afterglows 990123 and 021211 imply a WR lifetime $R_*/v_{sh} = 3 \times 10^4$ and 2×10^3 yr, respectively, i.e. much shorter than predicted by evolutionary models for such stars.

Having found some support for the wind-bubble scenario in the stalled WR wind-bubble model of Chevalier et al. (2004), and less so in the interaction between the RSG/LBV and WR winds, we proceed with testing it against the radio and optical observations of the afterglows 990123 and 021211. The wind-bubble scenario must satisfy the constraints given in Section 4.1, the first three pertaining to the emission from the fireball interacting with the homogeneous portion of the CBM, while the last three refer to the FS propagating in the r^{-2} bubble (instead of the 'RS', as indicated in those equations). In addition, the constraint

$$\nu_c^{(FS)}(t_1, t_4) > 5 \times 10^{14}\,\mathrm{Hz} \tag{65}$$

must be imposed, to explain the decrease of the afterglow dimming rate at t_*, when the uniform medium is encountered. We note that, for $s = 2$, ν_c increases in time, while for $s = 0$ it decreases. Thus,

if condition (65) is satisfied, then $\nu_c^{(FS)}$ is above the optical domain for any $t \in (t_1, t_4)$. We also note that this scenario has only four parameters, two (E and A_*) for the FS dynamics and two (ε_i and ε_B) for the emission. The density of the uniform region of the CBM is determined by the compression by a factor of 4 of the wind density at the location of the termination shock. From equation (64), we obtain that this density is

$$n_{s=0} = \frac{10^{36}\,A_*}{R_{*,\mathrm{cm}}^2} = 6 \times 10^3\,\frac{A_*^2}{E_{53}}\left(\frac{t_*}{600\,\mathrm{s}}\frac{2}{1+z}\right)^{-1}\,\mathrm{cm^{-3}}. \tag{66}$$

The density jump across the termination shock should lead to a brief brightening of the afterglow (Wijers 2001). Such a behaviour may have been missed in the afterglow 990123, where there is a gap in the optical observations from 10 min to 4 h. It is not seen in the optical measurements of the afterglow 021211 at the 'break' time of 10 min determined by Li et al. (2003); instead, an optical emission brighter by 0.5 mag than the double power-law fit used there is seen at 2 h after the burst. The lack of a brightening at the right time in the afterglow 021211 may be problematic for the wind-bubble scenario considered here.

Figs 4 and 5 display separately the FS microphysical parameters which accommodate the observations before and after t_*, for a few combinations of fireball energy E and wind parameter A_*. Smaller values of the former parameter or larger values for the latter do not allow the FS to accommodate the $t > t_*$ radio and optical emission of the afterglows 990123 and 021211. Note that, because the RS emission has at least one free parameter (τ and Γ_0), requiring that it does not exceed the measured optical fluxes or the radio upper limits, it does not constrain the FS parameters.

As shown in Fig. 4, the parameters ε_i and ε_B satisfying the observational constraints cannot be constant across R_* for the afterglow 990123, with the electron energy parameter increasing by a factor of $\gtrsim 100$ and the magnetic field parameter decreasing by a factor of $\gtrsim 100$ when the fireball crosses the wind termination shock. A similar conclusion is reached for the afterglow 021211 (Fig. 5).

6 CONCLUSIONS

We have investigated two scenarios that can account for the behaviour of the early optical emission of GRB afterglows 990123
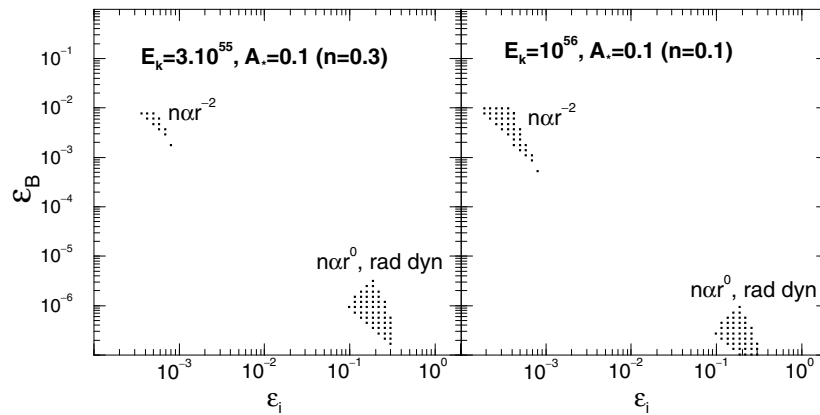

Figure 4. Wind-bubble scenario, GRB 990123. Forward shock microphysical parameters are shown separately for the wind-like, inner region of the CBM (marked '$n \propto r^{-2}$'), corresponding to the early, fast decaying, optical afterglow ($t < 650$ s), and the homogeneous, outer part of the CBM (denoted by '$n \propto r^0$'), where the $t > 4$ h, slower falling-off emission arises. These solutions were calculated assuming radiative dynamics, which is consistent with the resulting values of the microphysical parameters for $n \propto r^0$. Each panel indicates the fireball kinetic energy E, the wind parameter A_* and the resulting density n (equation 66) of the uniform outer medium. There are no solutions for the the $n \propto r^0$ region for denser winds or lower fireball energies. The lack of overlap between the wind and uniform medium solutions indicates that this scenario requires the parameters for magnetic field and minimal electron energy behind the FS to vary when the wind-bubble termination shock is encountered.
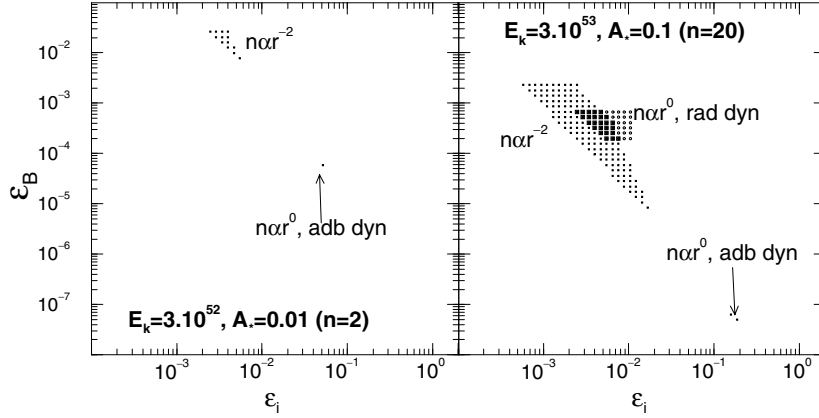
Figure 5. Wind-bubble scenario, GRB 021211. Same as in Fig. 4 but for the afterglow 021211. The allowed regions for the microphysical parameters for the wind and uniform portions of the CBM are shown. In the left panel, the assumption of adiabatic dynamics is justified by the resulting total electron energy $\epsilon_e = (p-1)\varepsilon_i/(p-2) = 5\,\varepsilon_i < 0.1$ for the required electron distribution index $p = 2.25$. In the right panel, for the homogeneous CBM region, neither dynamical regime is consistent with the microphysical parameters shown, thus the correct $n \propto r^0$ solutions should lie somewhere between the two extreme regimes, most likely not overlapping with the wind ($n \propto r^{-2}$) solutions.

and 021211, whose light curves fall-off as $t^{-1.7\pm0.1}$ at $t < t_* \simeq$ 600 s, while the decay at $t > t_*$ follows $t^{-1.0\pm0.1}$. The first scenario is the widely used reverse–forward shock scenario, where the fast decay of the early optical emission is attributed to the GRB ejecta energized by the RS, and the slower decaying phase is associated with CBM swept-up by the FS.

Fig. 1 shows that, for a homogeneous medium, the reverse–forward shock scenario can accommodate the radio and optical measurements of the afterglow 990123 if the ejecta magnetic field is $\gtrsim 10$ times larger than in the shocked CBM, which implies an ejecta frozen-in magnetic field (Mészáros & Rees 1997; Zhang et al. 2003), and if the RS parameter for the typical electron energy is $\gtrsim 10$ times smaller than for the FS. These differences between the microphysical parameters behind the two shocks are too large to be explained away by the inaccuracies in the calculations of the afterglow emission presented in Section 3.

For a wind-like CBM (Fig. 2), the reverse–forward shock scenario can explain the major properties of the radio and optical emissions of the afterglow 990123 with the same microphysical parameters behind both shocks (Fig. 2), but it requires a wind density corresponding to a mass-loss rate to speed ratio less than 10^{-6} M$_\odot$ yr^{-1}/10^3 km s^{-1} (i.e. $A_* < 0.1$). We obtain a similarly tenuous wind also from modelling the broad-band data of the afterglow 990123 at $t > 0.2$ d, but it should be noted that the best fit with a wind-like CBM provides a poorer fit to the data than a uniform medium.

Within the framework of the reverse–forward shock scenario, the same microphysical parameters are obtained for the afterglow 021211, for a thick ejecta shell and either a uniform or a wind-like CBM (the latter case is shown in Fig. 3). For a uniform CBM, we obtain $n \gtrsim 30$ cm^{-3}, larger than the $n \lesssim 1$ cm^{-3} inferred by us (Kumar & Panaitescu 2003) for a thin ejecta shell. For a wind-like CBM, the afterglow 021211 requires a wind density corresponding to a mass-loss rate to speed ratio below 10^{-6} M$_\odot$ yr^{-1}/10^3 km s^{-1}, a result similar to that obtained for the afterglow 990123.

The second scenario considered in this work (Section 5), that of the wind bubble having an inner r^{-2} wind-like region surrounded by a zone of uniform density, is motivated by the fact that the decrease in the dimming rate of the optical afterglows 990123 and 021211 seen at $t_* \sim 650$ s matches fairly well the expectations for such a density profile. The required CBM structure finds support

in the scenario of WR wind bubbles stalled by a high interstellar pressure as discussed by Chevalier et al. (2004). For this scenario to explain the general properties of the radio and optical emissions of the afterglows 990123 and 021211, the magnetic field and electron energy parameters would have to decrease and increase, respectively, by a factor of about 100 at $t = t_*$, when the wind termination shock is reached (Figs 4 and 5), a contrived feature without a physical foundation. We also find that the wind-bubble scenario requires winds which are as tenuous as those for the reverse–forward shock scenario.

Thus, the reverse–forward shock scenario provides a more natural explanation than the wind-bubble scenario for the steep early decay of the optical emission of the afterglows 990123 and 021211. Given that the GRB ejecta can be initially magnetized and that the RS is less relativistic than the FS, the microphysical parameters might differ behind the two shocks. If their equality is required for a simpler scenario, with fewer assumptions, then a wind-like CBM is favoured by the reverse–forward shock scenario, although a problem still exists: the low wind density inferred in each case ($A_* < 0.1$), which is similar to that derived by Chevalier et al. (2004) for the afterglows 020405 and 021211 and by Price et al. (2002) for the afterglow 011211. In the sample of 64 Galactic WR stars analysed by Nugis & Lamers (2000) there is only one star with $A_* < 0.1$, the majority of the other stars having a mass-loss rate $\dot{M} \in (0.5\text{–}7) \times 10^{-5}$ M$_\odot$ yr^{-1}, a wind velocity $v_w \in (1000\text{–}3000)$ km s^{-1} and $A_* \in (0.5, 3)$. The dependence of the mass-loss rate on stellar mass and metallicity inferred by Nugis & Lamers (2000) led to $\dot{M} \sim 10^{-6}(M/\text{M}_\odot)^{1.1}Y^{2.2}$ M$_\odot$ yr^{-1} for WN stars and $\dot{M} \sim 10^{-5}(M/\text{M}_\odot)^{1.1}Y^2 Z$ M$_\odot$ yr^{-1} for WCs, which may suggest that the tenuous winds required by the reverse–forward shock scenario for the afterglows 990123 and 021211 arise from WR stars which are less massive and less metal-rich than Galactic WRs (Wijers 2001; Chevalier et al. 2004). If such stars do not exist, then either the microphysical parameters must be different behind the RS crossing the GRB ejecta and the FS sweeping up the CBM or the fast declining early optical emission of the afterglows 990123 and 021211 is not arising in the RS. One possibility is that the early optical afterglow emission is produced in internal shocks occurring in an unsteady wind (Mészáros & Rees 1999), a scenario which was not investigated in this paper.

REFERENCES

Akerlof C. et al., 1999, Nat, 398, 400
Blandford R., McKee C., 1976, Phys. Fluids, 19(8), 1130
Castor J., McCray R., Weaver R., 1975, ApJ, 200, L107
Chevalier L., Imamura J., 1983, ApJ, 270, 554
Chevalier L., Li Z.-Y., 2000, ApJ, 536, 195
Chevalier L., Li Z.-Y., Fransson C., 2004, ApJ, 606, 369
Fox D. et al., 2003, ApJ, 586, L5
Garcia-Segura G., Mac Low M.-M., Langer N., 1996a, A&A, 305, 229
Garcia-Segura G., Langer N., Mac Low M.-M., 1996b, A&A, 316, 133
Holland S., Bjornsson G., Hjorth J., Thomsen B., 2000, A&A, 364, 467
Kobayashi S., Sari R., 2000, ApJ, 542, 819
Kulkarni S. et al., 1999a, ApJ, 522, L97
Kulkarni S. et al., 1999b, Nat, 398, 389
Kumar P., Panaitescu A., 2003, MNRAS, 346, 905
Li W., Filippenko A., Chornock R., Jha S., 2003, ApJ, 586, L9
Mészáros P., Rees M., 1997, ApJ, 476, 232
Mészáros P., Rees M., 1999, MNRAS, 306, L39
Mészáros P., Laguna P., Rees M. J., 1993, ApJ, 415, 181
Nugis T., Lamers H., 2000, A&A, 360, 227
Pandey S., Anupama G. C., Sagar R., Bhattacharya D., Castro-Tirado A. J., Sahu D. K., Parihar P., Prabhu T. P., 2003, A&A, 408, L21
Panaitescu A., Kumar P., 2000, ApJ, 543, 66
Panaitescu A., Kumar P., 2001, ApJ, 560, L49
Price P. et al., 2002, ApJ, 572, L51
Ramirez-Ruiz E., Dray L., Madau P., Tout C., 2001, MNRAS, 327, 829
Rees M. J., Mészáros P., 1994, ApJ, 430, L93
Sari R., Piran T., 1995, ApJ, 455, L143
Sari R., Piran T., 1999, ApJ, 517, L109
Sari R., Piran T., Narayan R., 1998, ApJ, 497, L17
Scalo J., Wheeler J., 2001, ApJ, 562, 664
Soderberg A., Ramirez-Ruiz E., 2003, MNRAS, 345, 854
Vreeswijk P., Fruchter A., Hjorth J., Kouveliotou C., 2002, GCN Circ., 1785
Wijers R., 2001, in Costa E., Frontera F., Jorth J., eds, Gamma-Ray Bursts in the Afterglow Era. Springer-Verlag, Berlin, p. 306
Wijers R., Galama T., 1999, ApJ, 523, 177
Zhang B., Kobayashi S., Mészáros P., 2003, ApJ, 595, 950

This paper has been typeset from a TEX/LATEX file prepared by the author.